EES Solar

PAPER

View Article Online
View Journal | View Issue

Cite this: *EES Sol.*, 2026, **2**, 456

Novel dopant-free carbazole- and phenothiazine-appended indolo[3,2-*a*]carbazole-based small molecules as efficient hole-transport materials for perovskite solar cells

Haritha Jalaja Raghavan,[a] Nideesh Perumbalathodi,[b] Jith C. Janardhanan,[c] Kala Kannankutty,[b] Madambi Kunjukuttan Ezhuthachan Jayaraj,[cd] Tzu-Chien Wei *[be] and Narayanapillai Manoj *[acd]

Developing efficient, stable, cost-effective hole-transport materials (HTMs) is critical for advancing high-performance perovskite solar cells (PSCs). In this study, we introduced novel, dopant-free fused heterocyclic indolo[3,2-*a*]carbazole (IC)-based HTMs, namely, C_{12}Cbz-IC and C_{12}Phz-IC, which are functionalized with electron-donating carbazole (Cbz) and phenothiazine (Phz) moieties, respectively. These IC-based HTMs are synthesized *via* a cost-effective Buchwald–Hartwig amination and exhibit superior hole mobility, enhanced hydrophobicity, and low-lying HOMO energy levels (−5.4 eV for C_{12}Cbz-IC and −5.5 eV for C_{12}Phz-IC). These characteristics facilitate efficient hole extraction and charge transport in PSCs. When incorporated into PSCs without dopants, C_{12}Cbz-IC and C_{12}Phz-IC achieved impressive power conversion efficiencies of 16.41% and 15.43%, respectively. A key advantage of these materials is their significantly low production cost, ∼50% that of the benchmark Spiro-OMeTAD-based HTM. Furthermore, stability tests demonstrated that after 1000 hours of dark storage, Spiro-OMeTAD-based devices retained only 34% of their initial efficiency, whereas C_{12}Cbz-IC and C_{12}Phz-IC maintained 51% and 54% of their initial efficiency, respectively. These findings highlight the potential of IC-based HTMs as cost-effective and stable alternatives to Spiro-OMeTAD, offering a promising pathway toward the development of next-generation, high-efficiency PSCs.

Received 24th January 2026
Accepted 30th January 2026

DOI: 10.1039/d6el00007j

rsc.li/EESSolar

Broader context

The large-scale commercialization of perovskite solar cells (PSCs) critically depends on the development of hole-transport materials (HTMs) that simultaneously deliver high efficiency, long-term stability, and low manufacturing cost. While state-of-the-art organic HTMs such as Spiro-OMeTAD enable high laboratory efficiencies, their reliance on costly synthesis routes, dopants, and limited intrinsic stability poses significant barriers to industrial deployment. In this study, we introduce fused heterocyclic indolo[3,2-*a*]carbazole (IC)-based HTMs, C_{12}Cbz-IC and C_{12}Phz-IC, synthesized *via* a cost-effective Buchwald–Hartwig amination strategy. These dopant-free HTMs combine favorable energy-level alignment, high hole mobility, and enhanced hydrophobicity, enabling efficient charge extraction and improved device stability. PSCs employing C_{12}Cbz-IC and C_{12}Phz-IC achieve power-conversion efficiencies of 16.41% and 15.43%, respectively while reducing material costs to approximately 50% of the benchmark Spiro-OMeTAD. Notably, the IC-based HTMs also exhibit superior operational stability, retaining over 50% of their initial efficiency after 1000 h of dark storage, compared to 34% for Spiro-OMeTAD. These results highlight the promise of rationally designed, dopant-free organic HTMs as a viable pathway toward cost-effective and stable PSC technologies suitable for large-scale implementation.

1. Introduction

Perovskite solar cells (PSCs) have emerged as a leading technology in photovoltaic research, demonstrating immense potential as next-generation photovoltaics. Their exceptional photogenerated carrier characteristics have led to a remarkable increase in power conversion efficiency (PCE), from 3.8% in 2009 to more than 25% at present.[1–4] In PSCs, the hole-transport material (HTM) plays a critical role in facilitating hole extraction and transport, suppressing charge recombination losses, and thereby enhancing overall device stability.[5–7] An ideal HTM

[a]*Department of Applied Chemistry Cochin University of Science and Technology, Kochi-22, India. E-mail: manoj.n@cusat.ac.in*

[b]*Department of Chemical Engineering National Tsing Hua University, 101, Section 2, Kuang Fu Road, Hsinchu, Taiwan 30013, Republic of China*

[c]*Inter-University Centre for Nanomaterials and Devices, Cochin University of Science and Technology, Kochi-22, India*

[d]*Centre of Excellence in Advanced Materials, Cochin University of Science and Technology, Kochi-22, India*

[e]*Research Center for Critical Issues, Academia Sinica, Taipei, Taiwan, Republic of China. E-mail: tcwei@mx.nthu.edu.tw*

must exhibit excellent carrier mobility, minimal visible-light absorption, and well-matched energy levels with the valence-band edge of the perovskite (PVSK) absorber to ensure optimal performance.[8–10] The most commonly used organic HTMs in PSCs are 2,2′,7,7′-tetrakis[*N*,*N*-di(*p*-methoxyphenyl) aminomethoxyphenyl]amino-9,9′-spirobifluorene (Spiro-OMeTAD) and poly[bis(*p*-phenyl)-2,4,6-trimethylphenyl]amine (PTTA). Spiro-OMeTAD, with an optical bandgap of 2.9 eV, has the highest occupied molecular orbital (HOMO) and lowest unoccupied molecular orbital (LUMO) energy levels of −5.2 eV and −2.3 eV, respectively, which is favorable for the extraction of hole from the PVSK absorber.[11] However, its orthogonal spiro-fluorene structure limits the extended π-conjugation across the donor moieties and prevents efficient π–π stacking in the film form. Additionally, propeller-type triphenylamine units increase the molecule's overall volume, creating large intermolecular distances. This results in poor hole mobility ($\sim 10^{-5}$ cm^2 V^{-1} s^{-1}) and low electrical conductivity ($\sim 10^{-8}$ S cm^{-1}) for the pristine films in the undoped form.[12] Despite these limitations, the hole mobility and conductivity of Spiro-OMeTAD can be enhanced through doping with hygroscopic salts, such as lithium bis(trifluoromethanesulfonic) imide (LiTFSI) and tris (2-(1*H*-pyrazol-1-yl)-4-*tert*-butylpyridine) cobalt (III)tri(bis(trifluoromethane)sulfonimide) (FK209). These dopants improve charge transport *via* p-doping, which involves charge transfer between the dopant molecules and Spiro-OMeTAD.[13–15] However, these hygroscopic dopants also accelerate PVSK degradation by absorbing moisture from the environment, thereby reducing the lifespan and stability of PSCs. Additionally, as dopants are not covalently bound to the HTM and are ionic, they can undergo ion diffusion under an electric field, further degrading PCE and stability.[16–19]

Aside from stability concerns, Spiro-OMeTAD is prohibitively expensive (~$568 per g from Sigma) due to its complex multi-step synthesis and purification process, making it unsuitable for large-scale PSC fabrication.[9,20] The high production cost, combined with the poor long-term stability of doped HTMs, poses significant challenges in the commercialization of devices based on this material. Consequently, there is a growing demand for dopant-free HTMs that offer both cost-effectiveness and improved stability while maintaining high PCEs in PSCs.[6,21]

Among emerging molecular frameworks, carbazole (Cbz) and phenothiazine (Phz) cores have garnered significant attention due to their strong electron-donating properties, structural planarity, and facile functionalization. Carbazole derivatives exhibit high thermal stability and deep HOMO levels, making them excellent candidates for an efficient hole extraction in perovskite solar cells (PSCs). Liu *et al.* designed a star-shaped carbazole HTM (LD29), achieving a dopant-free PCE of 14.3%, demonstrating the potential of carbazole π-systems to replace doped Spiro-OMeTAD. Positional isomers such as Cz-4T-TPA have also been developed to enhance conjugation and reduce energetic disorder, achieving efficiencies exceeding 19%. LD29, incorporating triphenylamine side arms, exhibits a deep HOMO level (−5.24 eV), high hole mobility (1.72×10^{-5} cm^2 V^{-1} s^{-1}), good film-forming ability, and relatively high glass-transition temperature (121 °C). Dopant-free PSCs based on LD29 reached a PCE of 14.29%, while doped devices achieved over 18%, comparable to spiro-OMeTAD. Owing to its low synthesis cost, concentration-insensitive performance, and favorable stability, LD29 is a promising HTM for scalable PSC applications.[22] Wang *et al.* later introduced methoxy-substituted carbazole analogues (CZ-OMeTPA), which improved film homogeneity and yielded a PCE of 17.1%.[23,24] Rakstys *et al.* developed positional isomers (Cz-4T-TPA) that enhanced conjugation and reduced energetic disorder, achieving efficiencies above 19%.[25] El Fakir *et al.* studied six carbazole-based small molecules, including two reported molecules (M1 and M2) and four newly designed derivatives substituted at the 3,6- and 2,7-positions with the methoxyphenyl (P1, P2) and dimethoxyphenylamine (E1, E2) groups. DFT and TD-DFT calculations, along with frontier orbital alignment and reorganization energy analyses, identified M1, P1/2, and E1/2 as favorable HTMs, while M2 displayed a preferential electron transport behavior. This work highlights the importance of substitution patterns in governing charge separation and transport efficiency.[26] Nazeeruddin *et al.* designed two structural isomers of triarylamine-substituted carbazole HTMs to investigate the effect of substitution patterns on optoelectronic and photovoltaic properties. The 2,7-linked isomer (Car[2,3]) exhibited red-shifted absorption, high thermal stability (>420 °C), and favorable HOMO alignment with the perovskite valence band. PSCs employing Car[2,3] achieved a PCE of 19.23% and retained over 80% of their initial efficiency after 1000 h of continuous illumination, underscoring the importance of molecular planarity and substitution geometry.[27] Furthermore, Nazeeruddin and co-workers developed branched carbazole-based HTMs containing varying numbers of 3,6-bis(4,4′-dimethoxydiphenylamino)carbazole (Cz-OMeDPA) units linked by aliphatic chains. These amorphous materials exhibited high thermal stability (T_g > 120 °C) and hole mobilities up to 3.1×10^{-5} cm^2 V^{-1} s^{-1}, comparable to spiro-OMeTAD. PSCs employing optimized HTMs achieved PCEs of ~20% with a slightly improved device stability, highlighting the effectiveness of molecular branching.[28] Yang *et al.* replaced conventional heterocyclic cores with sulfonyldibenzene units in carbazole-based HTMs (3,6-SFY and 2,7-SFY), resulting in improved film quality and device performance. The corresponding PSCs delivered PCEs of 19.02% and 20.29%, respectively, with mixed-isomer devices retaining 91% of their initial efficiency, demonstrating the effectiveness of rational structural engineering.[29] Lu and co-workers further developed carbazole-based non-spiro small-molecule HTMs by introducing a hydrophobic trifluoropropoxy terminal group into SGT-405(3,6). The optimized HTM, SGT-405s(C_2,CF_3), exhibited high hole mobility (3.32×10^{-4} cm^2 V^{-1} s^{-1}), high glass-transition temperature (183 °C), and enhanced hydrophobicity, enabling PSCs with a PCE of 20.14%, outperforming spiro-OMeTAD while maintaining improved thermal and long-term stability.[30] These studies confirm that carbazole frameworks enable stable, dopant-free hole transport with tunable optoelectronic properties.

In parallel, phenothiazine-based HTMs have demonstrated excellent performance due to their unique S–N heterocyclic

structure, which promotes charge delocalization and oxidation stability. Grätzel and co-workers reported three phenothiazine-based HTMs with donor substituents 4,4-dimethyltriphenylamine (Z28), *N*-ethylcarbazole (Z29), and 4,4-dimethoxytriphenylamine (Z30) linked through vinylene bridges. Z30 delivered the highest PCE of 19.17%, whereas Z29 showed a lower PCE of 17.77% due to insufficient hole-extraction driving force and reduced hole mobility.[31] Salunke *et al.* developed low-cost phenothiazine-based HTMs, AZO-I and AZO-II, functionalized with azomethine groups. PSCs employing these materials achieved PCEs of 14.3% and 15.6%, respectively, highlighting their potential as cost-effective alternatives.[32]

Robertson *et al.* reported triphenylbenzene (TPB)-core-based HTMs, TPB(2-MeOTAD) and phenothiazine-substituted TPB(2-TPTZ), synthesized *via* low-cost Buchwald–Hartwig coupling. The phenothiazine incorporation resulted in red-shifted absorption and favorable HOMO alignment with $MAPbI_3$. While TPB(2-TPTZ) exhibited lower PCE than TPB(2-MeOTAD), it demonstrated superior thermal and operational stability, retaining 85% of its initial efficiency after 300 h.[33] Tsang's group developed dopant-free phenothiazine-based D–π–D HTMs (BDT-PTZ and BDT-POZ) for p–i–n PSCs. The fused thiophene-bridged donor architecture enabled efficient charge transport and favorable energy-level alignment with $MAPbI_3$. BDT-POZ exhibited higher hole mobility (2.1×10^{-4} cm^2 V^{-1} s^{-1}), more efficient hole extraction, and reduced charge recombination, achieving a PCE of 19.16% with minimal hysteresis, outperforming PTAA.[34] To further reduce HTM costs, Robertson developed a series of spiro[fluorene-9,9′-xanthene] (SFX)-based HTMs (SFX-TAD, SFX-TCz, SFX-TPTZ, and SFX-MeOTAD) *via* Buchwald–Hartwig amination. These materials exhibited suitable optical absorption and tunable HOMO levels (−5.70 to −5.10 eV). Deeper HOMO levels in SFX-TAD and SFX-TPTZ contributed to higher open-circuit voltages, demonstrating the effectiveness of SFX-based frameworks for a cost-efficient HTM design.[35] Zhao's group further developed SFX-core-based HTMs, SFX-PT1 and SFX-PT2, which exhibited suitable optical absorption (~321 nm), tunable HOMO levels (−5.08 to −5.20 eV), and excellent thermal stability. Notably, SFX-PT1 displayed high hole mobility (2.08×10^{-3} cm^2 V^{-1} s^{-1}), surpassing both SFX-PT2 and spiro-OMeTAD, underscoring the effectiveness of SFX-based molecular engineering for high-performance HTMs.[36] Collectively, these molecular design strategies underscore that both carbazole and phenothiazine scaffolds can rival or surpass Spiro-OMeTAD in terms of efficiency, scalability, and stability.

In this context, we designed indolo[3,2-*a*]carbazole (IC)-based, small-molecule, dopant-free HTMs (C_{12}Cbz-IC and C_{12}Phz-IC), incorporating electron-rich moieties (ERMs), such as carbazole (Cbz) and phenothiazine (Phz), through a cost-effective three-step synthetic route. The ERMs were introduced in a manner that preserves the favorable HOMO/LUMO energy levels of the parent indolo [3,2-*a*]carbazole (IC).[37] In the benchmark HTM Spiro-OMeTAD, orthogonally oriented diarylamine donors prevent direct conjugation with the central indacene π-system. A similar molecular design strategy was employed here, wherein heterocyclic units are positioned orthogonally to the IC core. Specifically, Cbz and Phz groups were appended to the orthogonal phenyl rings at the C_6 and C_7 positions of the IC[3,2-*a*] framework of C_{12}Cbz-IC and C_{12}Phz-IC, respectively, yielding a molecular topology analogous to that of Spiro-OMeTAD. Furthermore, a long alkyl chain (*n*-$C_{12}H25$) was introduced at the heterocyclic N-atoms of the IC core to enhance solubility and improve thin-film morphology. This rational molecular design integrates the superior electronic properties of carbazole and phenothiazine donors with the IC core, aiming to achieve cost-effective, thermally stable, and highly efficient dopant-free HTMs suitable for scalable PSC.

2. Experimental

2.1 Fabrication of the electron-transporting material (ETM)

A 3 × 3 cm piece of fluoride-doped tin oxide (FTO) glass (thickness 2.2 mm, sheet resistance 8 Ω sq^{-1}, Dyesol) was patterned using a laser machine (690 nm, LMF-020F, Laser Life Company, Taiwan). Then, the patterned substrate was cleaned in several steps: first, it was immersed in a 4% solution of a commercial detergent (PK-LCG46, Parker International Co. Ltd., Taiwan) in RO water and sonicated for 30 minutes. Second, the substrate was rinsed thoroughly with DI water and dried using a hot air gun. After a 10-minute treatment with UV/ozone, a compact TiO_2 (c-TiO_2) layer was spin-coated onto the cleaned FTO using a 0.3 M solution of titanium dissopropoxide bis(acetylacetonate) (75% in 2-propanol, Sigma-Aldrich). The solution was spun at 4000 rpm for 30 seconds, followed by heating at 120 °C for 5–10 minutes. Subsequently, the coated substrates were annealed at 500 °C for 1 h. Once cooled to room temperature, the substrates were soaked in a 40 mM aqueous solution of $TiCl_4$ (98%, Fluka), maintained at 70 °C for 30 minutes, rinsed with deionized water and ethanol, and dried using an air blow gun.

For the mesoporous TiO_2 (m-TiO_2) layer, a diluted paste (30 NR-D, Dyesol) in ethanol (1 : 7 weight ratio) was spin-coated at 6000 rpm for 30 seconds. The resulting film was heated at 120 °C for 5–10 minutes and then annealed at 500 °C. After cooling to room temperature, the compact and mesoporous TiO_2 films were sectioned into 1.5 × 1.5 cm pieces and treated again with a 40 mM $TiCl_4$ solution at 70 °C for 30 minutes. After rinsing with deionized water and drying, the films were sintered at 500 °C for 1 h. Finally, after cooling to 150 °C, the substrates were transferred to a humidity-controlled environment (10–15% RH) for subsequent PVSK layer deposition.

2.2 Fabrication of the PVSK

PVSK film is prepared using a single-step deposition method, in which the PVSK precursor is prepared by mixing 1.5 M PbI_2 (99.9%, Alfa Aesar), 0.1 M $PbBr_2$ (99.9%, Alfa Aesar), 1.2 M formamidinium iodide (FAI, 99.8%, Lumtec), 0.1 M methylammonium bromide (MABr, 99.9%, Lumtec), and 0.5 M methylammonium chloride (MACl, 99.9%, Lumtec) in a solvent mixture of DMF and DMSO (4 : 1 volume ratio), resulting in a molar composition of $FA_{0.66}MA_{0.34}PbI_{0.93}Br_{0.07}$.[38,39] This

solution was spin-coated in two stages: first at 1000 rpm for 10 seconds and then at 6000 rpm for 20 seconds. During the high-speed step, 130 μL of chlorobenzene was dripped onto the substrate 10 seconds before the end. The coated films were then heated sequentially at 150 °C and 100 °C for 10 minutes to facilitate the crystal growth of PVSK.

2.3 Fabrication of the hole-transporting material (HTM) and gold electrode

The Spiro-OMeTAD-based HTM solution was formulated by dissolving 32 mM lithium bis(trifluoromethane sulfonyl)imide (Li-TFSI, >99.9%, Sigma-Aldrich) and 195 mM *tert*-butylpyridine (*t*BP, 96%, Sigma-Aldrich) in chlorobenzene (99.8%, Sigma-Aldrich), followed by stirring at room temperature for 24 h. Subsequently, Spiro-OMeTAD (99.5%, Lumtec) was added to this pre-solvent to achieve a final concentration of 75 mM. This HTM solution was spin-coated onto the FTO/ETM/PVSK substrate at 4000 rpm for 20 seconds. The HTM-coated substrate was then stored overnight in a dark, low-humidity environment (RH = 10–15%) to allow for proper oxidation of Spiro-OMeTAD HTM. For IC-based-HTMs, C_{12}Cbz-IC and C_{12}Phz-IC, solutions were prepared by dissolving 20 mg of each compound in chlorobenzene, followed by stirring at 80 °C for 4 h to ensure complete dissolution. The HTM solutions were preheated at 60 °C for 30 minutes before they were dynamically spin-coated onto the FTO/ETM/PVSK substrate at 4000 rpm for 30 seconds. Finally, an 80 nm-thick gold electrode was thermally evaporated onto the HTM layer to complete the device assembly.

3. Result and discussion

3.1 Synthesis of 6,7-bis(4-(9*H*-carbazol-9-yl) phenyl)-5,12-didodecyl-5,12-dihydroindolo [3,2-*a*] carbazole (1, C_{12}Cbz-IC)

The reaction involves (Scheme 1) the Buchwald–Hartwig amination reaction of compound **3**, (which was synthesized by an acid-catalysed condensation reaction)[40] (1 eq.) with carbazole (6, 3 eq.) in the presence of sodium *tert*-butoxide (4 eq.), tri-*tert*-butylphosphine (10 mol%) and palladium acetate (10 mol%) in DCM. After the solvent was removed *in vacuo*, the residue was purified *via* silica gel column chromatography (100–120 mesh, hexane–DCM solvent mixture). The product was obtained as

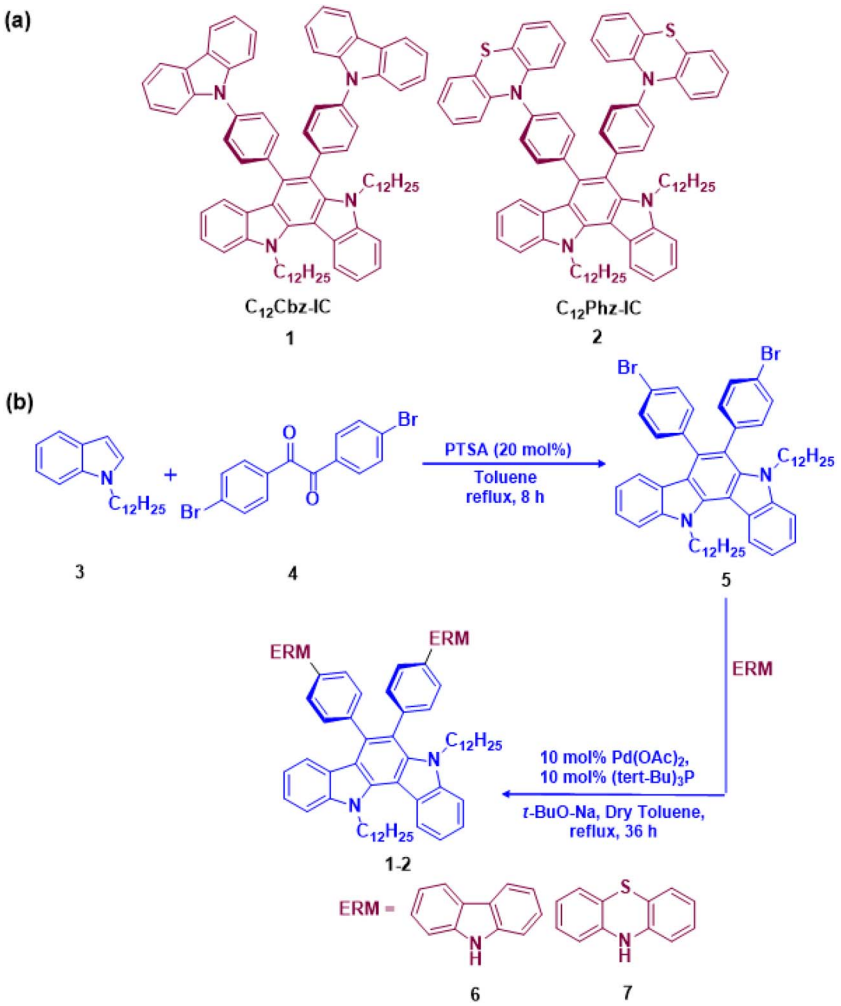

Scheme 1 (a) Structure of C_{12}Cbz-IC and C_{12}Phz-IC HTMs used in this study. (b) Synthetic routes of C_{12}Cbz-IC and C_{12}Phz-IC HTMs.

a colourless solid with ~78% yield (detailed ^{1}H NMR and ^{13}C NMR are provided in the SI, Fig. S1–S4).

3.2 Synthesis of 10,10′-((5,12-didodecyl-5,12-dihydroindolo [3,2-*a*] carbazole-6,7-diyl) bis(4,1-phenylene)) bis(10*H*-phenothiazine) (2, C_{12}Phz-IC)

The same Buchwald–Hartwig amination reaction (Scheme 1) was involved with compound **3**, (1 eq.) and phenothiazine (7, 3 eq.) in the presence of sodium *tert*-butoxide (4 eq.), tri-*tert*-butylphosphine (10 mol%) and palladium acetate (10 mol%) in DCM. After the solvent was removed *in vacuo*, the residue was purified *via* silica gel column chromatography (100–120 mesh, hexane–DCM solvent mixture). A colourless crystalline solid with ~75% yield was obtained (detailed ^{1}H NMR and ^{13}C NMR are provided in Fig. S5 and S8).

The hole extraction efficiency of HTMs is critically governed by interfacial energy-level alignment. In particular, the HOMO level or valence band maximum of the HTM should be positioned slightly above that of the PVSK layer to facilitate efficient hole transfer while suppressing interfacial recombination. To evaluate the electronic structure, its structural correlation, and the suitability of the HTM, theoretical calculations using quantum mechanical density functional theory (DFT) calculations (B3LYP/6311G (d, p)) were performed using the Gaussian 09 software.[41] Optimized geometries were further used in the calculations of the molecular electrostatic potential surface (ESP) to map the electron-rich and electron-deficient domains in the molecule. The optimized geometric structure of the model molecules C_{12}Cbz-IC and C_{12}Phz-IC is shown in Fig. 1. From the optimized geometry of the C_{12}Cbz-IC, it was observed that the interconnecting phenyl rings lie orthogonal to the planes of the IC framework and the carbazole/phenothiazine planes. The dihedral angle (ϕ_1) between the plane of the indolo[3,2-*a*] framework (from left) and the phenyl ring is 80°, and that of the second phenyl ring (ϕ_2) is 85° (Fig. 1a). In the case of C_{12}Phz-IC 89° and 82° for ϕ_1 and ϕ_2, respectively, the dihedral angles (Fig. 1b) are observed (Table S1). Thus, this unique positioning of the bridging phenyl ring between the IC framework and the electron-rich Cbz/Phz leads to minimal electronic coupling and perturbation of HOMO/LUMO levels. This ensures overall higher electron density, which is desirable for an HTM material.

The computed energies of the HOMO and the LUMO are presented in Table S2. The value obtained for the HOMO level (C_{12}Cbz-IC ~−5.36 eV and C_{12}Phz-IC ~−5.16 eV) implies a matching energy-level characteristic with that of Spiro-OMeTAD (−5.17 eV).[42] The contours of the HOMO and LUMO surfaces are presented in Fig. 1c and d. The HOMO of C_{12}Cbz-IC is mainly localized on the indolo [3, 2-*a*]carbazole framework (Fig. 1c), while in the case of C_{12}Phz-IC, the HOMO is mainly localized on the phenothiazine unit and on the bridging phenyl ring (Fig. 1d). The LUMO surface, however, is localized on the indolocarbazole framework for all the prepared compounds. This suggests a possible intramolecular charge transfer transition as the important electronic transition responsible for the absorption spectral properties. Fig. 1e and f depicts the molecular electrostatic potential distribution of C_{12}CbzIC and C_{12}PhzIC, respectively. The negative charge is mainly distributed on the main plane of the indolocarbazole unit as well as the donor unit. On the other hand, the positive charge is mainly concentrated on the twisted phenyl groups of the indolocarbazole framework.[37] This implies no direct conjugation between the donor groups and the indolocarbazole unit.

The normalized UV-vis absorption and photoluminescence (PL) spectra of C_{12}Cbz-IC and C_{12}Phz-IC HTMs in THF solution are presented in Fig. 2a and b, respectively, while the absorbance and transmittance of the corresponding HTM films on FTO substrates are shown in Fig. 2c and d. In the solution state (Fig. 2a), C_{12}Cbz-IC and C_{12}Phz-IC exhibit distinct absorption

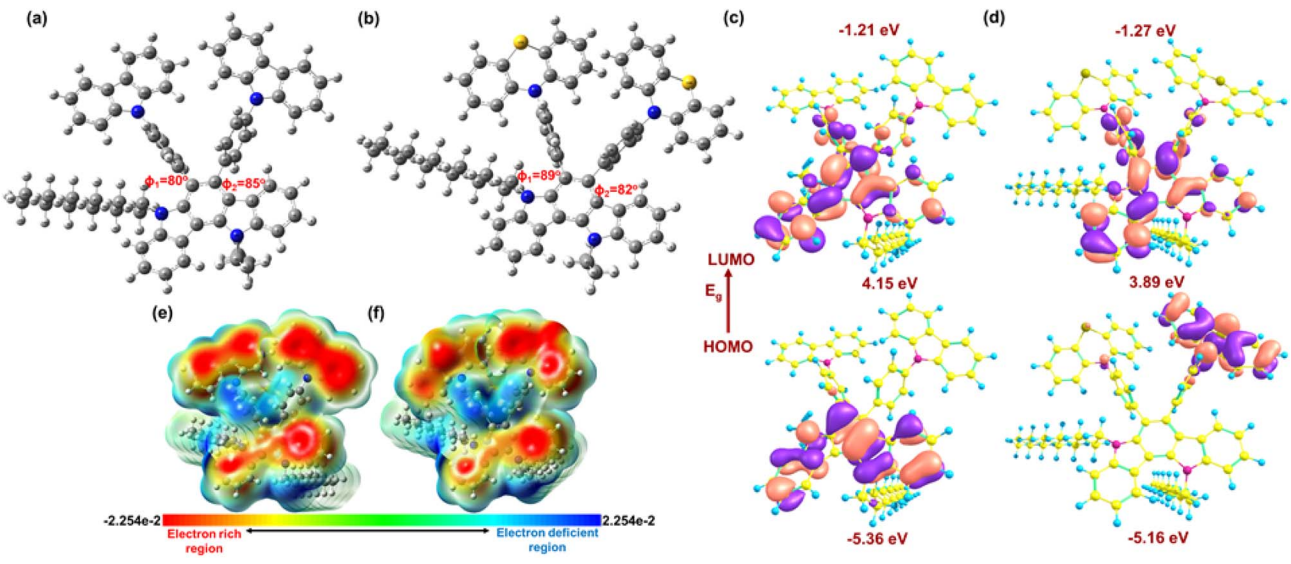

Fig. 1 (a) Optimized structures of the model molecules (a) C_{12}Cbz-IC and (b) C_{12}Phz-IC. (c) Energy-level structures of C_{12}Cbz-IC and (d) C_{12}Phz-IC. (e). Electrostatic potential surface images of C_{12}Cbz-IC and (f) C_{12}Phz-IC.

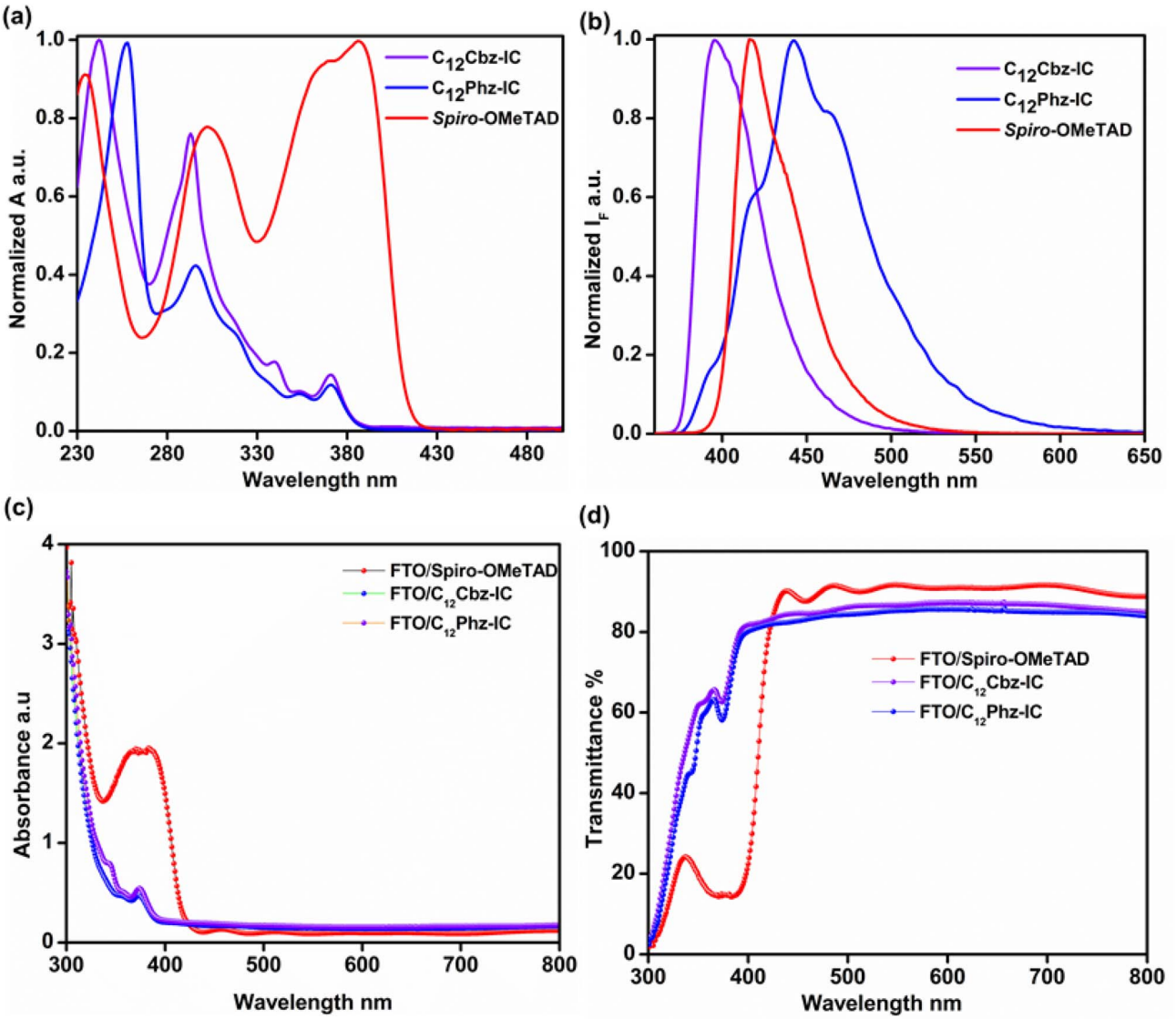

Fig. 2 (a) Normalized UV-vis absorption spectra and (b) photoluminescence spectra of C_{12}Cbz-IC and C_{12}Phz-IC were recorded in a 10^{-5} M THF solution. (c) UV-vis absorption spectra of the C_{12}Cbz-IC and C_{12}Phz-IC HTM films on FTO. (d) Transmittance spectra of the C_{12}Cbz-IC, C_{12}Phz-IC, and Spiro-OMeTAD thin films on FTO.

bands centred at ~242 nm and 258 nm, respectively, along with a weak absorption shoulder around 371 nm. These absorption characteristics, without any significant absorption in the visible region of the spectrum, ensure higher transparency in the visible region suitable for ideal HTMs. The emission spectra, recorded upon excitation at 340 nm (Fig. 2b), reveal a broad photoluminescence peak at ~395 nm for C_{12}Cbz-IC, whereas C_{12}Phz-IC displays a red-shifted emission at ~440 nm. The optical band gaps (E_g), determined from the intersection of the absorption and emission spectra, range between 3.20 and 3.25 eV (Fig. S9 and Table 1).

Grazing-incidence X-ray diffraction (GI-XRD) was employed to examine the molecular packing and preferred orientation of the dopant-free HTMs C_{12}Cbz-IC and C_{12}Phz-IC deposited on FTO substrates (Fig. S10). For the C_{12}Cbz-IC film (Fig. S10a), the GI-XRD θ–2θ pattern shows a discernible reflection at $2\theta \approx 20.24°$, corresponding to a d-spacing of ≈4.38 Å. This spacing is characteristic of short-range intermolecular ordering in π-conjugated organic semiconductors and is commonly associated with close core–core packing rather than long-range alkyl-chain-driven lamellar assembly. Notably, no pronounced low-angle reflection is observed in the range typically associated with lamellar packing (≈8–25 Å), indicating that extended lamellar segregation is suppressed in the C_{12}Cbz-IC film on FTO. The higher-angle reflections observed at ~33.9°, 38.0°, 51.8°, and 62.1° originate from the FTO substrate and are therefore excluded from the analysis of HTM ordering. These features suggest a relatively molecular arrangement with limited long-range ordering but appreciable short-range π-core packing, consistent with reports on carbazole-based small-molecule semiconductors on polar oxide substrates.[43,44] In contrast, the GI-XRD pattern of the C_{12}Phz-IC film (Fig. S10b)

Table 1 Cyclic voltammetry analysis data of HTMs

HTM	[a]E_{ox} *vs.* Fc/Fc$^+$ (V)	[b]HOMO (IP)/eV	[c]LUMO (EA)/eV vacuum	[d]E_{0-0} (eV)
C_{12}Cbz-IC	0.66	−5.46	−2.21	3.25
C_{12}Phz-IC	0.73	−5.15	−1.95	3.20
Spiro-OMeTAD	0.56	−5.36	−2.30	3.06

[a] The oxidative onset potential (E_{ox} *vs.* Fc/Fc$^+$) was measured *via* CV in acetonitrile. [b] HOMO = −[4.8 + (E_{ox} − Fc/Fc$^+$)]. [c] $E_{LUMO} = E_{HOMO} - E_{0-0}$. [d] Energy gap calculated from the intersection of absorption and emission maxima.

exhibits a distinct low-angle reflection at $2\theta \approx 10.59°$, corresponding to a *d*-spacing of ≈8.35 Å, which is assigned to lamellar molecular packing arising from the periodic segregation of the long C_{12} alkyl chains and π-conjugated indolo[3,2-*a*]carbazole cores. The presence of this lamellar reflection in the specular geometry indicates preferential alignment of the lamellar planes parallel to the substrate, evidencing a higher degree of out-of-plane molecular ordering. A weaker feature at $2\theta \approx 19.7°$ ($d \approx 4.5$ Å) is attributed to a secondary packing periodicity associated with tilted or offset core arrangements within the lamellar structure. As for C_{12}Cbz-IC, higher-angle peaks are dominated by diffraction from the FTO substrate. The more pronounced lamellar ordering observed for C_{12}Phz-IC can be rationalized by the increased molecular rigidity and steric differentiation introduced by the phenothiazine-based peripheral units, which promote alkyl-chain segregation and layered self-assembly, consistent with prior studies on alkylated small-molecule organic semiconductors and HTMs.[45–47]

In the thin-film state, both C_{12}Cbz-IC and C_{12}Phz-IC HTMs exhibit negligible absorption in the visible region, starkly contrasting with the benchmark HTM, Spiro-OMeTAD, which shows significant visible-light absorption. The high optical transparency of C_{12}Cbz-IC and C_{12}Phz-IC HTMs in the film form makes them suitable as HTMs in PSC. Furthermore, the UV-vis spectra of PVSK films coated with these HTMs (Fig. 2c) confirm the absence of any additional parasitic absorption. The transmittance spectra of C_{12}Cbz-IC and C_{12}Phz-IC thin films (Fig. 2d) demonstrate transparency comparable to or superior to that of Spiro-OMeTAD films, reinforcing their potential, as their presence does not attenuate the transmission of visible light in PSC devices. HOMO energy levels must be suitably positioned to achieve an optimal balance between efficient hole transfer, maximizing the open-circuit voltage (V_{oc}) of the device.[48] The ground-state oxidation potentials of the HTMs, which are commonly used to estimate their HOMO energy levels, were determined *via* cyclic voltammetry (CV). In this study, the oxidation behaviour of C_{12}Cbz-IC and C_{12}Phz-IC was examined in acetonitrile using 0.1 M tetrabutylammonium tetrafluoroborate as the supporting electrolyte (Fig. 3a). Both HTMs exhibited two oxidation events, consistent with their electron-rich molecular structures. For the HOMO energy estimation, the first oxidation onset potential was used, as it corresponds to the initial electron removal process and is typically associated with the HOMO energy level. The HOMO energy levels calculated from these onset potentials were −5.46 eV for C_{12}Cbz-IC and −5.15 eV for C_{12}Phz-IC (Table 1 and Fig. 3b). The difference in the HOMO energies reflects the electronic nature of the substituents: the carbazole-based HTM exhibits a slightly deeper HOMO, whereas the phenothiazine-based analogue displays a somewhat shallower HOMO due to its stronger electron-donating character. Notably, these values are comparable to those of the benchmark HTM Spiro-OMeTAD (−5.36 eV).

Based on these energy levels, a PSC device architecture can be designed, as illustrated in Fig. 3c. In this configuration, the active PVSK layer, $FA_{0.66}MA_{0.34}PbI_{0.93}Br_{0.07}$, possesses a HOMO level of −5.80 eV.[49] This alignment facilitates efficient hole extraction from the PVSK layer toward the Au electrode. Such an

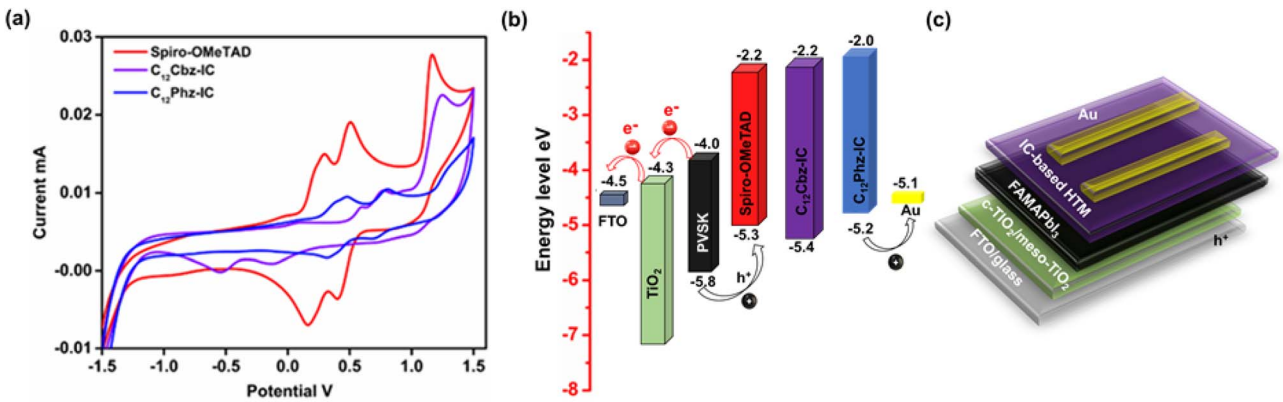

Fig. 3 (a) Cyclic voltammograms of the various IC-based and Spiro-OMeTAD HTMs, (b) device architecture of the PSC used in this study, and (c) energy-level diagram of different components in the PSC.

energy positioning ensures effective exergonic charge separation and carrier transport within the device. Additionally, the LUMO levels of C_{12}Cbz-IC and C_{12}Phz-IC (Table 1) are sufficiently high, preventing electron back-transfer from the PVSK layer. This characteristic is crucial for maintaining efficient charge extraction while minimizing recombination losses.

To further evaluate the film morphology of C_{12}Cbz-IC and C_{12}Phz-IC deposited on PVSK layers, scanning electron microscopy (SEM) was employed. As shown in Fig. S11a and b, both IC-based HTMs form a continuous layer over PVSK. Cross-sectional SEM images (Fig. S11c and d) of the FTO/PVSK/HTM stacks reveal that the C_{12}Cbz-IC layer exhibits an average thickness of ~95 nm, whereas the C_{12}Phz-IC layer has a slightly thinner average thickness of about 92 nm. Notably, small voids with lateral dimensions of ~20 nm are observed at the PVSK/HTM interface for both IC-based HTM samples (indicated by red circles). These interfacial voids are likely associated with the rapid crystallization of the IC-based HTMs during deposition from the chlorobenzene processing solvent, which may limit conformal interfacial contact with the PVSK layer.

The photovoltaic performance of PSCs incorporating C_{12}Cbz-IC and C_{12}Phz-IC as HTMs was evaluated using the standard FTO/TiO_2/$FAMAPbI_3$/HTM/Au device architecture. The undoped C_{12}Cbz-IC and C_{12}Phz-IC HTMs were tested under simulated AM 1.5G solar irradiation (100 mW cm^{-2}), and the resulting *J–V* curves under reverse scan are presented in Fig. 4a. A statistical analysis of the photovoltaic parameters for multiple devices using IC-based HTMs and Spiro-OMeTAD is provided in Fig. 4b–e. The benchmark device, employing the commercially available doped Spiro-OMeTAD HTM, demonstrated a high PCE of 20.45%, with a short current density (J_{sc}) of 23.79 mA cm^{-2}, a V_{oc} of 1.06 V, and a fill factor (FF) of 0.81. The PSC fabricated with C_{12}Cbz-IC achieved a PCE of 16.41%, with a J_{sc} of 21.91 mA cm^{-2}, a V_{oc} of 1.04 V, and an FF of 0.72. Similarly, the C_{12}Phz-IC-based PSC exhibited a PCE of 15.43%, a J_{sc} of 21.72 mA cm^{-2}, a V_{oc} of 1.03 V, and an FF of 0.69 (Table 2).

The hysteresis behavior of PSCs incorporating C_{12}Cbz-IC and C_{12}Phz-IC as HTMs was evaluated by measuring forward and reverse *J–V* characteristics under standard AM 1.5-G illumination (Fig. S12). The degree of hysteresis was quantified using the

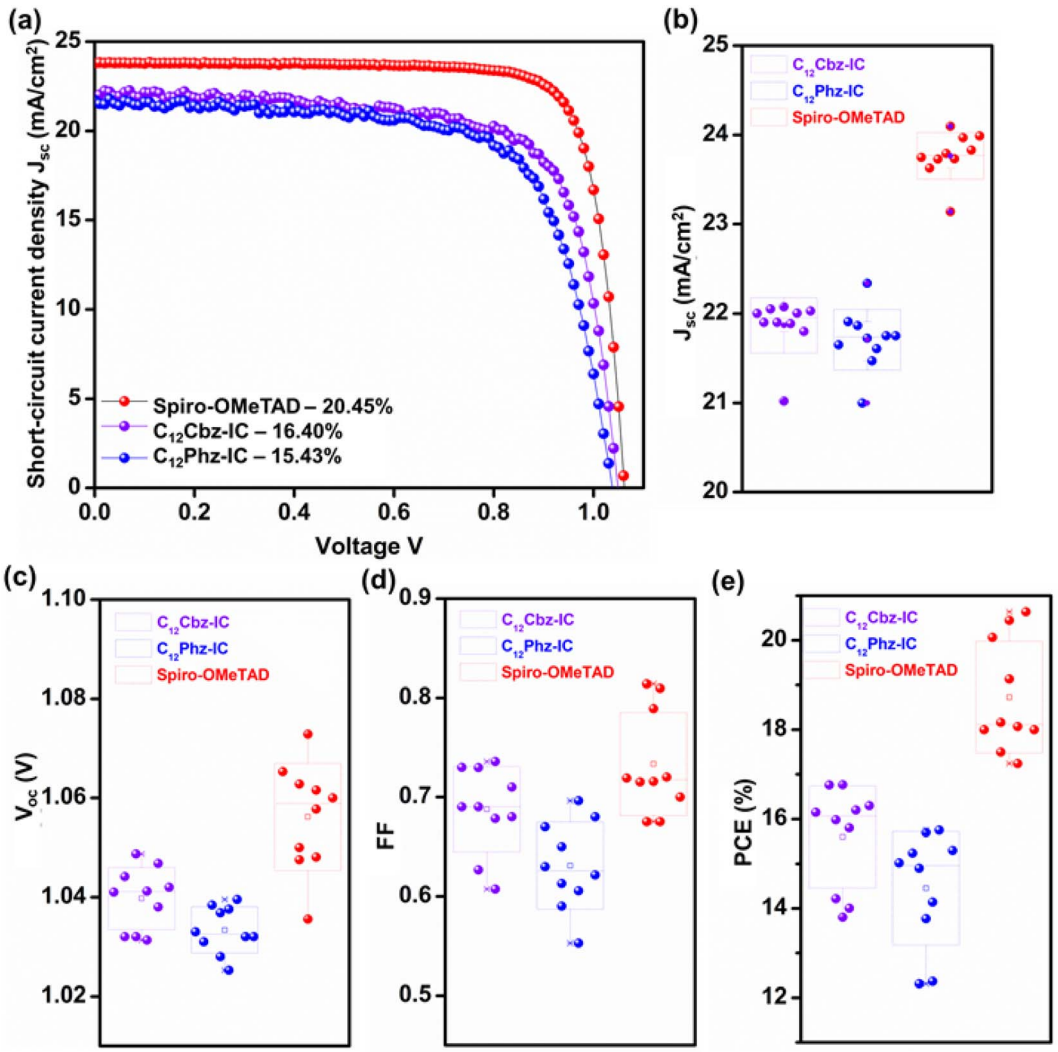

Fig. 4 (a) *J–V* curves of the champion PSCs (reverse scan), (b–e) statistical analysis of the photovoltaic parameters of different PSCs.

Table 2 Photovoltaic parameters of champion devices

HTM	J_{sc} (mA cm^{-2})	V_{oc} (V)	FF	PCE (%)
Spiro-OMeTAD	23.79	1.06	0.81	20.45
C_{12}Cbz-IC	21.91	1.04	0.72	16.41
C_{12}Phz-IC	21.72	1.03	0.69	15.43

hysteresis index (HI), calculated from the relative difference between the power-conversion efficiencies obtained from the backward and forward scans according to the following expression:[50–53]

$$\mathrm{HI} = \left|\frac{\mathrm{PCE}_{\mathrm{backward}} - \mathrm{PCE}_{\mathrm{forward}}}{\mathrm{PCE}_{\mathrm{backward}}}\right|$$

Devices based on C_{12}Cbz-IC exhibit a comparatively low hysteresis index (HI ≈ 0.05), reflecting an efficient and well-balanced charge extraction as well as suppressed interfacial charge trapping. In contrast, PSCs employing C_{12}Phz-IC show more pronounced hysteresis, with an HI of approximately 0.14. The higher hysteresis observed in C_{12}Phz-IC-based devices is likely associated with increased interfacial charge accumulation and less-efficient carrier transport relative to C_{12}Cbz-IC-based HTMs.

To gain insights into the charge transfer properties of the optimized IC-based HTMs, steady-state photoluminescence (SSPL) measurements were performed (Fig. 5a). The PVSK film exhibits strong PL emission, indicating high-quality film formation with minimal defects on the glass substrate. However, when IC-based HTMs are coated onto the PVSK layer, a significant quenching of PL intensity is observed for both IC-HTMs, indicating efficient hole extraction facilitated by these materials. A closer examination of the SSPL spectra for both C_{12}Cbz-IC and C_{12}Phz-IC revealed further reduction in PL intensity for C_{12}Cbz-IC compared with C_{12}Phz-IC, indicating the superior hole extraction capability of C_{12}Cbz-IC. Furthermore, the hole mobilities of the synthesized HTMs were estimated using the space-charge limited current (SCLC) method by fabricating hole-only devices (FTO/PEDOT:PSS/HTM/Au) and analyzing their dark *J–V* characteristics (Fig. 5b). The SCLC curve was fitted according to the Mott–Gurney law to determine hole mobility.[54]

$$(J) = \frac{9}{8}\mu\varepsilon\varepsilon_0\frac{V^2}{d^3}$$

where J is the current density, ε is the permittivity of the organic material (3), ε_0 is the vacuum permittivity (8.85 × 10^{-12} F m^{-1}), μ is the hole mobility, V is the applied voltage, and d is the thickness of the film. The obtained hole mobility values for the HTMs were 1.4 × 10^{-4} cm^2 V^{-1} s^{-1} for C_{12}Cbz-IC and 1.2 × 10^{-4} cm^2 V^{-1} s^{-1} for C_{12}Phz-IC, respectively, while the benchmark doped Spiro-OMeTAD exhibited a hole mobility of 4.1 × 10^{-3} cm^2 V^{-1} s^{-1}. This demonstrates the suitability of dopant-free IC-based HTMs for an efficient charge transport in PSC.[13,55,56]

Furthermore, the external quantum efficiency (EQE) of the IC-based HTM devices was measured over the wavelength range of 300 to 800 nm, as shown in Fig. S13. The integrated short-circuit current densities (J_{sc}) for the different films follow a trend similar to that observed in the *J–V* measurements (Fig. 4a). Specifically, the J_{sc} values for the C_{12}Cbz-IC and C_{12}Phz-IC devices were 21.91 mA cm^{-2} and 21.72 mA cm^{-2}, respectively. This correlation further supports the consistent performance of these devices, highlighting the comparable charge collection efficiency of IC-based HTMs without dopants.

The thermal stability of HTMs is crucial for the long-term performance of PSC. The thermal stability of the prepared HTMs was evaluated *via* thermogravimetric analysis (TGA) and differential scanning calorimetry (DSC) under a nitrogen (N_2) atmosphere. The results indicate that the degradation temperatures of C_{12}Cbz-IC and C_{12}Phz-IC are approximately 464 °C and 430 °C, respectively (Fig. 6a). These values demonstrate desirable thermal stability for application as HTMs in photovoltaic devices and are comparable to that of Spiro-OMeTAD (T_{dec} = 449 °C).[57] Fig. 6b presents the DSC thermograms of C_{12}Cbz-IC and C_{12}Phz-IC, showing peaks corresponding to the melting and glass transition processes, while no crystallization peak is detected. For C_{12}Cbz-IC, the melting temperature (T_m) is

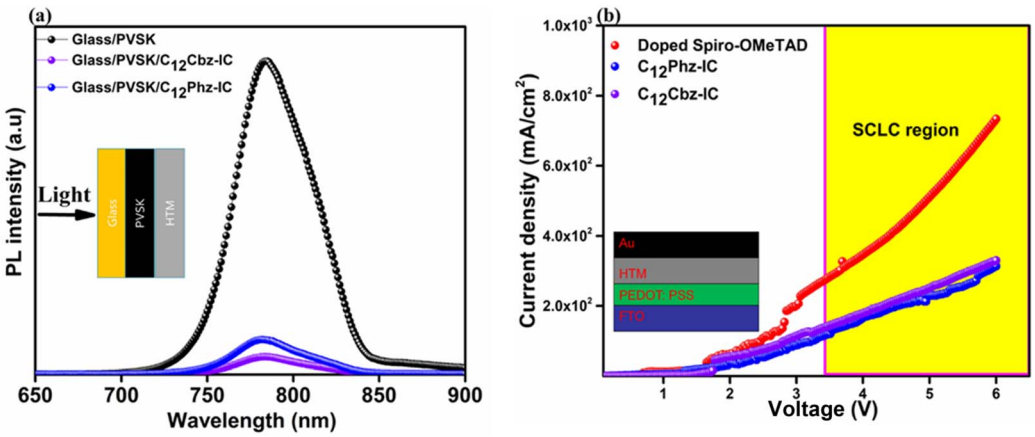

Fig. 5 (a) SSPL of the glass/PVSK, glass/PVSK/C_{12}Cbz-IC, and glass/PVSK/C_{12}Phz-IC films. (b) SCLC curve of the doped Spiro-OMeTAD, C_{12}Cbz-IC, and C_{12}Phz-IC.

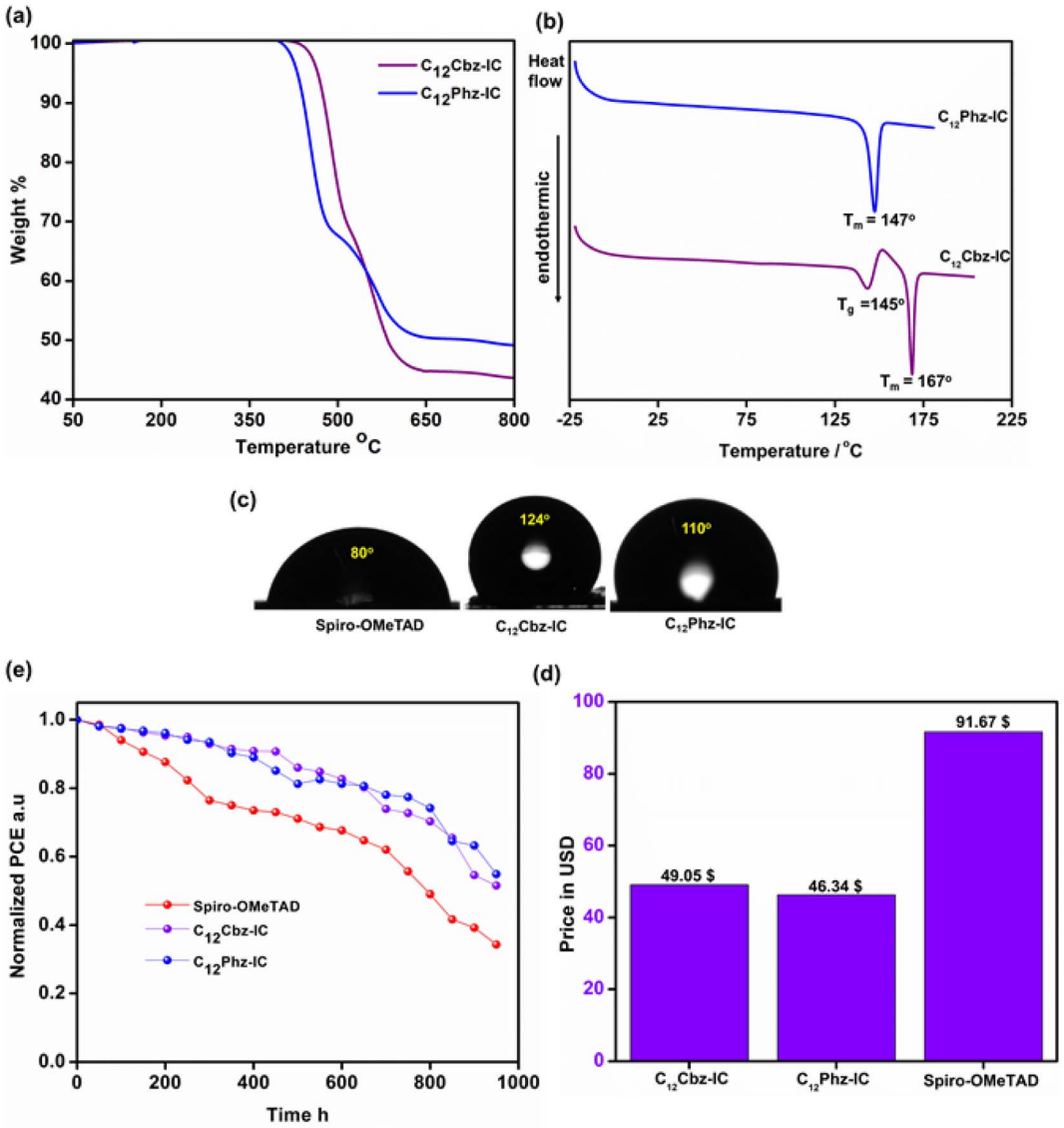

Fig. 6 (a) Thermogravimetric analysis of C_{12}Cbz-IC and C_{12}Phz-IC under nitrogen (N_2) atmosphere with a heating rate of 10 °C min^{-1}; (b) DSC curves for C_{12}Cbz-ICs and C_{12}Phz-IC, with a heating rate of 10 °C min^{-1} under nitrogen (N_2) atmosphere. (c) WCA of the thin films of Spiro-OMeTAD, C_{12}CbzICs and C_{12}PhzIC. (d) Long-term stability of the Spiro-OMeTAD and IC HTM-based PSCs. (e) Cost evaluation of Spiro-OMeTAD and different IC-based HTMs.

observed at 167 °C, whereas for C_{12}Phz-IC, the T_m is 147 °C. The DSC curve of C_{12}Cbz-IC reveals a glass transition temperature (T_g) of 145 °C, attributed to the presence of a long alkyl chain, indicating that C_{12}Cbz-IC can exist in both the crystalline and amorphous states. However, the glass transition temperature for C_{12}Phz-IC was not experimentally detected. Notably, no crystallization process was observed beyond T_g for both HTMs, suggesting a reduced tendency for crystallization. This reduced crystallization tendency is beneficial for forming high-quality thin films during device fabrication. To evaluate the hydrophobicity of the prepared HTMs, water contact angle (WCA) measurements were performed on the thin films of IC-based HTMs and Spiro-OMeTAD (Fig. 6c). The benchmark Spiro-OMeTAD exhibited a WCA of 80°. Interestingly, the newly developed IC-based HTMs, C_{12}Cbz-IC and C_{12}Phz-IC, demonstrated a significantly higher WCA of 124° and 110°, respectively, indicating superior hydrophobicity. This enhanced hydrophobicity is attributed to the presence of long alkyl chains on the heterocyclic core of the molecules. Improved water resistance is crucial for preventing moisture infiltration, which could otherwise compromise the stability of the PVSK active layer and degrade the device performance.

Furthermore, the long-term operational stability of PSCs employing doped Spiro-OMeTAD and undoped IC-based HTMs was systematically evaluated under dark storage conditions at 25 °C and a relative humidity of 15–20%, as presented in Fig. 6d. The device incorporating doped Spiro-OMeTAD exhibited rapid performance degradation, retaining only 34% of its initial PCE after 1000 hours of storage. In contrast, PSCs based on C_{12}Cbz-IC and C_{12}Phz-IC maintained 51% and 54% of their initial

efficiencies, respectively, demonstrating significantly enhanced stability relative to the benchmark Spiro-OMeTAD device. Despite the improved stability of the IC-based HTMs, their long-term performance remains partially limited by the non-uniform film coverage and the formation of voids at the PVSK/HTM interface, as revealed by the morphological analyses (Fig. S11c and d). Such interfacial defects can facilitate the gradual ingress of moisture or Au diffusion during prolonged storage, ultimately accelerating device degradation. Future efforts will therefore focus on optimizing film-forming properties to achieve highly uniform and defect-free IC-based HTM layers. The inferior stability of doped Spiro-OMeTAD-based devices is primarily attributed to the presence of hygroscopic Li-TFSI dopants, which promote moisture uptake and accelerate the chemical degradation of Spiro-OMeTAD, thereby hastening PVSK decomposition. In contrast, the dopant-free and intrinsically hydrophobic nature of IC-based HTMs serves as an effective moisture barrier, mitigating environmental degradation and enhancing device stability.

To further substantiate the superior moisture tolerance of IC-based HTMs, water immersion tests were performed by dipping pristine perovskite films, as well as Spiro-OMeTAD-, C_{12}Cbz-IC-, and C_{12}Phz-IC-coated PVSK films, in deionized water (DI) for 10 min (Fig. S14). The pristine PVSK film rapidly turned colourless upon immersion, indicating severe degradation. The UV-vis spectroscopy of the resulting solution revealed a pronounced absorption peak at ~260 nm after 10 min, corresponding to dissolved PbI_2 species. Notably, the PbI_2 concentration detected in water from C_{12}Cbz-IC- and C_{12}Phz-IC-coated PVSK films was substantially lower than that from the Spiro-OMeTAD-coated counterpart. These results indicate that the highly hydrophobic C_{12}Cbz-IC and C_{12}Phz-IC HTMs effectively suppress moisture-induced perovskite degradation and limit lead leaching, highlighting their superior protective capability and enhanced moisture tolerance.[58]

Additionally, Table 3 and Fig. 6e present a comparative evaluation of laboratory-scale synthesis costs for C_{12}Cbz-IC, C_{12}Phz-IC, and the benchmark HTM Spiro-OMeTAD.[59–61] The synthesis costs of C_{12}Cbz-IC and C_{12}Phz-IC were estimated using the current prices of chemical reagents from suppliers in India. The results of the cost analyses are presented in Tables S3 and S4 (SI). The cost of synthetic Spiro-OMeTAD was taken from previously reported literature, and its commercial price is also listed in Table 3. When both device efficiency and operational stability are considered, the overall cost of the new high-performance HTMs, C_{12}Cbz-IC and C_{12}Phz-IC, is about half that of synthetic Spiro-OMeTAD. This cost is expected to decrease further with large-scale synthesis. These results demonstrate the economic advantages of the dopant-free HTMs developed in this study and highlight their strong potential for cost-effective and stable PSC applications.

Table 3 Comparison of the lab synthesis costs of C_{12}Cbz-IC, C_{12}Phz-IC and Spiro-OMeTAD

Compound	Material cost [$ per g]	Commercial price [$ per g]
C_{12}Cbz-IC	49.05	—
C_{12}Phz-IC	46.34	—
Spiro-OMeTAD	91.67 (ref. 59–61)	568.31

4. Conclusion

In this study, we developed novel dopant-free organic HTMs, C_{12}Cbz-IC and C_{12}Phz-IC, based on a fused heterocyclic indolo[3,2-*a*]carbazole core. Both HTMs exhibit superior optical, thermal, and electrochemical properties, along with higher hole mobility, compared with the benchmark HTM Spiro-OMeTAD. PSCs incorporating undoped C_{12}Cbz-IC and C_{12}Phz-IC achieved PCEs of 16.41% and 15.43%, respectively, demonstrating competitive performance relative to doped Spiro-OMeTAD-based devices. Importantly, cost analysis revealed that the material costs of C_{12}Cbz-IC and C_{12}Phz-IC were ~50% lower than those of commercially available Spiro-OMeTAD on a per-gram basis, highlighting a clear economic advantage. Combined with their excellent intrinsic stability, high PCE, and reduced material cost, these IC-based HTMs represent promising alternatives to Spiro-OMeTAD for high-performance PSCs. Overall, this study provides a viable pathway toward sustainable, dopant-free HTM design, supporting the large-scale commercialization of cost-effective PSC technologies.

Author contributions

This work is part of the PhD thesis of HJR. NM and TCW supervised the study. HJR conceived the idea, designed the experiments, and wrote the first manuscript draft. NP contributed to experimental design, conducted the experiment, curated the data, and assisted with manuscript preparation. JCJ assisted with the Buchwald–Amination reaction. M. K. J. is one of the project's PIs, and Kala Kannankutty contributed to manuscript modification. All authors contributed to the writing and revision.

Conflicts of interest

The authors declare no competing interests.

Data availability

The data supporting this article have been included as part of the supplementary information (SI). Supplementary information is available. See DOI: https://doi.org/10.1039/d6el00007j.

Acknowledgements

H. J. R. gratefully acknowledges the University Grants Commission (UGC) for the research fellowship (55/(OBC) (CSIR-UGC NET DEC.2016)). N. M., M. K. J. and T. C. W. are thankful to DST – GITA (GITA/DST/TWN/p-85/2019) for financial support. This project has received funding from the National Science and Technology Council, ROC (NSTC 112-2221-E-007-013-MY3). The

authors are grateful to National Tsing Hua University (NTHU), Hsinchu, Rashtriya Uchchatar Shiksha Abhiyan (RUSA), DST-SAIF Cochin, IUCND CUSAT, CAM CUSAT, Department of Polymer Science and Rubber Technology CUSAT, and Department of Physics CUSAT for facilities.

References

1 M. M. Lee, J. Teuscher, T. Miyasaka, T. N. Murakami and H. J. Snaith, *Science*, 2012, **338**, 643–647.
2 J. W. Choi, B. Shin, P. Gorai, R. L. Z. Hoye and R. Palgrave, *ACS Energy Lett.*, 2022, **7**, 1553–1557.
3 E. Kabir, P. Kumar, S. Kumar, A. A. Adelodun and K.-H. Kim, *Renew. Sustain. Energy Rev.*, 2018, **82**, 894–900.
4 Z. Shen, Q. Han, X. Luo, Y. Shen, Y. Wang, Y. Yuan, Y. Zhang, Y. Yang and L. Han, *Nat. Photonics*, 2024, **18**, 450–457.
5 J.-P. Correa-Baena, W. Tress, K. Domanski, E. H. Anaraki, S.-H. Turren-Cruz, B. Roose, P. P. Boix, M. Grätzel, M. Saliba, A. Abate and A. Hagfeldt, *Energy Environ. Sci.*, 2017, **10**, 1207–1212.
6 Z. H. Bakr, Q. Wali, A. Fakharuddin, L. Schmidt-Mende, T. M. Brown and R. Jose, *Nano Energy*, 2017, **34**, 271–305.
7 J. Liu, Y. Wu, C. Qin, X. Yang, T. Yasuda, A. Islam, K. Zhang, W. Peng, W. Chen and L. Han, *Energy Environ. Sci.*, 2014, **7**, 2963–2967.
8 N. J. Jeon, H. G. Lee, Y. C. Kim, J. Seo, J. H. Noh, J. Lee and S. Il Seok, *J. Am. Chem. Soc.*, 2014, **136**, 7837–7840.
9 F. M. Rombach, S. A. Haque and T. J. Macdonald, *Energy Environ. Sci.*, 2021, **14**, 5161–5190.
10 Q. Chen, J. Wu, X. Wang, Y. Yang, Y. Du, Z. Li, X. Zhang, Z. Zhang, W. Pan and W. Sun, *Electrochem. Commun.*, 2021, **126**, 107020.
11 H.-S. Kim, C.-R. Lee, J.-H. Im, K.-B. Lee, T. Moehl, A. Marchioro, S.-J. Moon, R. Humphry-Baker, J.-H. Yum, J. E. Moser, M. Gratzel and N.-G. Park, *Sci. Rep.*, 2012, **2**, 591.
12 H. Min, D. Y. Lee, J. Kim, G. Kim, K. S. Lee, J. Kim, M. J. Paik, Y. K. Kim, K. S. Kim, M. G. Kim, T. J. Shin and S. Il Seok, *Nature*, 2021, **598**, 444–450.
13 H. J. Snaith and M. Grätzel, *Appl. Phys. Lett.*, 2006, **89**, 262114.
14 W. Wang, J. Zhou and W. Tang, *J. Mater. Chem. A*, 2022, **10**, 1150–1178.
15 S.-G. Kim, S.-H. Lee, I. S. Yang, Y.-J. Park, K. Park, J.-W. Lee and N.-G. Park, *ACS Energy Lett.*, 2022, **7**, 741–748.
16 Z. Li, C. Xiao, Y. Yang, S. P. Harvey, D. H. Kim, J. A. Christians, M. Yang, P. Schulz, S. U. Nanayakkara, C.-S. Jiang, J. M. Luther, J. J. Berry, M. C. Beard, M. M. Al-Jassim and K. Zhu, *Energy Environ. Sci.*, 2017, **10**, 1234–1242.
17 P. J. Linstrom and W. G. Mallard, *NIST Chemistry WebBook*, 2011.
18 Z. Hawash, L. K. Ono, S. R. Raga, M. V Lee and Y. Qi, *Chem. Mater.*, 2015, **27**, 562–569.
19 A. K. Jena, M. Ikegami and T. Miyasaka, *ACS Energy Lett.*, 2017, **2**, 1760–1761.
20 X. Zhao and N.-G. Park, *Photonics*, 2015, **2**(4), 1139–1151.
21 L. Calió, S. Kazim, M. Grätzel and S. Ahmad, *Angew. Chem., Int. Ed.*, 2016, **55**, 14522–14545.
22 X. Liu, X. Ding, Y. Ren, Y. Yang, Y. Ding, X. Liu, A. Alsaedi, T. Hayat, J. Yao and S. Dai, *J. Mater. Chem. C*, 2018, **6**, 12912–12918.
23 Y. Wang, X. Chen, J. Shao, S. Pang, X. Xing, Z. Dong, S. Liu, Z. Cui, X. Deng and C. Shi, *Sol. Energy*, 2019, **190**, 361–366.
24 P. Gratia, A. Magomedov, T. Malinauskas, M. Daskeviciene, A. Abate, S. Ahmad, M. Grätzel, V. Getautis and M. K. Nazeeruddin, *Angew. Chem., Int. Ed.*, 2015, **54**, 11409–11413.
25 K. Rakstys, S. Paek, A. Drevilkauskaite, H. Kanda, S. Daskeviciute, N. Shibayama, M. Daskeviciene, A. Gruodis, E. Kamarauskas, V. Jankauskas, V. Getautis and M. K. Nazeeruddin, *ACS Appl. Mater. Interfaces*, 2020, **12**, 19710–19717.
26 Z. El Fakir, A. Idrissi, A. Habsaoui and S. Bouzakraoui, *J. Mol. Graph. Model.*, 2023, **122**, 108504.
27 A. A. Sutanto, V. Joseph, C. Igci, O. A. Syzgantseva, M. A. Syzgantseva, V. Jankauskas, K. Rakstys, V. I. E. Queloz, P.-Y. Huang, J.-S. Ni, S. Kinge, A. M. Asiri, M.-C. Chen and M. K. Nazeeruddin, *Chem. Mater.*, 2021, **33**, 3286–3296.
28 P. Luizys, J. Xia, M. Daskeviciene, K. Kantminiene, E. Kasparavicius, H. Kanda, Y. Zhang, V. Jankauskas, K. Rakstys, V. Getautis and M. K. Nazeeruddin, *Chem. Mater.*, 2021, **33**, 7017–7027.
29 Y. Yang, S. Un Ryu, F. Wu, H. Lu, K. Jia, C. Zhong, T. Park and L. Zhu, *Chem. Eng. J.*, 2021, **424**, 130396.
30 C. Lu, M. Aftabuzzaman, C. Hoon Kim and H. Kyu Kim, *Chem. Eng. J.*, 2022, **428**, 131108.
31 F. Zhang, S. Wang, H. Zhu, X. Liu, H. Liu, X. Li, Y. Xiao, S. M. Zakeeruddin and M. Grätzel, *ACS Energy Lett.*, 2018, **3**, 1145–1152.
32 J. Salunke, X. Guo, Z. Lin, J. R. Vale, N. R. Candeias, M. Nyman, S. Dahlström, R. Österbacka, A. Priimagi, J. Chang and P. Vivo, *ACS Appl. Energy Mater.*, 2019, **2**, 3021–3027.
33 M. R. Maciejczyk, R. Chen, A. Brown, N. Zheng and N. Robertson, *J. Mater. Chem. C*, 2019, **7**, 8593–8598.
34 Y. Chen, X. Xu, N. Cai, S. Qian, R. Luo, Y. Huo and S.-W. Tsang, *Adv. Energy Mater.*, 2019, **9**, 1901268.
35 M. Maciejczyk, A. Ivaturi and N. Robertson, *J. Mater. Chem. A*, 2016, **4**, 4855–4863.
36 X. Liang, C. Wang, M. Wu, Y. Wu, F. Zhang, Z. Han, X. Lu, K. Guo and Y.-M. Zhao, *Tetrahedron*, 2017, **73**, 7115–7121.
37 H. J. Raghavan, N. Perumbalathodi, L. Tom, K. Kannankutty, M. K. E. Jayaraj, N. Manoj and T.-C. Wei, *Mater. Adv.*, 2024, **5**, 6925–6935.
38 T.-S. Su, T.-E. Fan, H.-K. Si, D.-A. Le, N. Perumbalathodi and T.-C. Wei, *Sol. RRL*, 2021, **5**, 2100109.
39 N. Perumbalathodi, T.-S. Su, Z.-F. He, K. Kannankutty and T.-C. Wei, *ACS Appl. Energy Mater.*, 2024, **7**(9), 3656–3666.
40 V. Nair, V. Nandialath, K. G. Abhilash and E. Suresh, *Org. Biomol. Chem.*, 2008, **6**, 1738–1742.
41 K. S. Keremane, I. M. Abdellah, P. Naik, A. El-Shafei and A. V. Adhikari, *Phys. Chem. Chem. Phys.*, 2020, **22**, 23169–23184.

42 H. Ashassi-Sorkhabi and P. Salehi-Abar, *Sol. Energy*, 2018, **173**, 132–138.
43 R. Noriega, J. Rivnay, K. Vandewal, F. P. V Koch, N. Stingelin, P. Smith, M. F. Toney and A. Salleo, *Nat. Mater.*, 2013, **12**, 1038–1044.
44 J. Filo and M. Putala, *J. Electr. Eng.*, 2010, **61**, 314–320.
45 L. Wang, S. Guo, K. Zhou and W. Ma, *Sustain. Energy Fuels*, 2020, **4**, 4934–4955.
46 G. Nan, Q. Shi, Z. Shuai and Z. Li, *Phys. Chem. Chem. Phys.*, 2011, **13**, 9736–9746.
47 G.-W. Kim, G. Kang, J. Kim, G.-Y. Lee, H. Il Kim, L. Pyeon, J. Lee and T. Park, *Energy Environ. Sci.*, 2016, **9**, 2326–2333.
48 S. Vegiraju, W. Ke, P. Priyanka, J.-S. Ni, Y.-C. Wu, I. Spanopoulos, S. L. Yau, T. J. Marks, M.-C. Chen and M. G. Kanatzidis, *Adv. Funct. Mater.*, 2019, **29**, 1905393.
49 N. Perumbalathodi, T.-S. Su and T.-C. Wei, *Adv. Mater. Interfaces*, 2022, **9**, 2201191.
50 D.-A. Le, K. Kala, T.-S. Su, N. Perumbalathodi and T.-C. Wei, *Sol. RRL*, 2024, 2400553.
51 S. N. Habisreutinger, N. K. Noel and H. J. Snaith, *ACS Energy Lett.*, 2018, **3**, 2472–2476.
52 S. A. L. Weber, I. M. Hermes, S.-H. Turren-Cruz, C. Gort, V. W. Bergmann, L. Gilson, A. Hagfeldt, M. Graetzel, W. Tress and R. Berger, *Energy Environ. Sci.*, 2018, **11**, 2404–2413.
53 G. A. Sepalage, S. Meyer, A. Pascoe, A. D. Scully, F. Huang, U. Bach, Y.-B. Cheng and L. Spiccia, *Adv. Funct. Mater.*, 2015, **25**, 5650–5661.
54 Y. Su, H. Li, Y. Miao, Y. Tian and M. Cheng, *Asian J. Org. Chem.*, 2022, **11**, e202200441.
55 J. Zhang, B. Xu, M. B. Johansson, N. Vlachopoulos, G. Boschloo, L. Sun, E. M. J. Johansson and A. Hagfeldt, *ACS Nano*, 2016, **10**, 6816–6825.
56 J. Y. Park, S. L. Kwak, H. J. Park and D.-H. Hwang, *Nanomaterials*, 2023, **13**(3), 1934.
57 H. D. Pham, S. M. Jain, M. Li, Z.-K. Wang, S. Manzhos, K. Feron, S. Pitchaimuthu, Z. Liu, N. Motta, J. R. Durrant and P. Sonar, *Adv. Electron. Mater.*, 2020, **6**, 1900884.
58 J. Zhang, T. Liu, Z. Bao, H. Liu, Y. Lv, X. Guo, X. Liu, Y. Chang and B. Li, *Chem. Eng. J.*, 2023, **459**, 141573.
59 H. D. Pham, T. T. Do, J. Kim, C. Charbonneau, S. Manzhos, K. Feron, W. C. Tsoi, J. R. Durrant, S. M. Jain and P. Sonar, *Adv. Energy Mater.*, 2018, **8**, 1703007.
60 T. Malinauskas, M. Saliba, T. Matsui, M. Daskeviciene, S. Urnikaite, P. Gratia, R. Send, H. Wonneberger, I. Bruder, M. Graetzel, V. Getautis and M. K. Nazeeruddin, *Energy Environ. Sci.*, 2016, **9**, 1681–1686.
61 T. K. T. Tu, S. A. Salma, M. Jeong, J. H. Kim, Y. T. Jeong, Y.-S. Gal and K. T. Lim, *Macromol. Res.*, 2021, **29**, 735–742.